ANTIMICROBIAL AGENTS AND CHEMOTHERAPY, July 2009, p. 3065–3073 Vol. 53, No. 7
0066-4804/09/$08.00+0 doi:10.1128/AAC.01666-08

Crystal Structure of *Bacillus anthracis* Dihydrofolate Reductase with the Dihydrophthalazine-Based Trimethoprim Derivative RAB1 Provides a Structural Explanation of Potency and Selectivity▽†

Christina R. Bourne,[1]* Richard A. Bunce,[2] Philip C. Bourne,[1] K. Darrell Berlin,[2] Esther W. Barrow,[1] and William W. Barrow[1]*

Department of Veterinary Pathobiology, 250 McElroy Hall,[1] and Department of Chemistry, Physical Sciences I,[2] Oklahoma State University, Stillwater, Oklahoma 74078

Received 18 December 2008/Returned for modification 3 February 2009/Accepted 6 April 2009

Bacillus anthracis **possesses an innate resistance to the antibiotic trimethoprim due to poor binding to dihydrofolate reductase (DHFR); currently, there are no commercial antibacterials that target this enzyme in *B. anthracis*. We have previously reported a series of dihydrophthalazine-based trimethoprim derivatives that are inhibitors for this target. In the present work, we have synthesized one compound (RAB1) displaying favorable 50% inhibitory concentration (54 nM) and MIC (≤12.8 μg/ml) values. RAB1 was cocrystallized with the *B. anthracis* DHFR in the space group $P2_12_12_1$, and X-ray diffraction data were collected to a 2.3-Å resolution. Binding of RAB1 causes a conformational change of the side chain of Arg58 and Met37 to accommodate the dihydrophthalazine moiety. Unlike the natural substrate or trimethoprim, the dihydrophthalazine group provides a large hydrophobic anchor that embeds within the DHFR active site and accounts for its selective inhibitory activity against *B. anthracis*.**

Bacillus anthracis has emerged as a relevant pathogen in regard to homeland security, and national stockpiles of therapeutics are being sought (www.bt.cdc.gov/Stockpile/). Currently available therapies are ciprofloxacin, tetracyclines, and penicillin (35); no available dihydrofolate reductase (DHFR) inhibitors are indicated for anthrax. This presents an ideal situation for combating possible future events since the *B. anthracis* DHFR is not currently targeted therapeutically. Therefore, any malicious alterations to the organism would presumably not affect this untargeted bacterial DHFR enzyme. We sought here to utilize this target by structure-aided design of selective inhibitors for *B. anthracis* DHFR.

Unlike their eukaryotic counterparts, prokaryotes cannot absorb dietary folate and possess a de novo folate synthesis pathway. This results in folate utilization, requiring the action of DHFR to carry out NADPH-dependent oxidation of dihydrofolate (FAH_2) to tetrahydrofolate. DHFR is found in both prokaryotes and eukaryotes, and all DHFR enzymes studied to date are targeted by the chemotherapeutic methotrexate (MTX) (40). Selectivity can be achieved, such as targeting plasmodial organisms with pyrimethamine (2). In addition, some prokaryotic DHFR's are selectively inhibited by trimethoprim (TMP) (13, 28, 51).

Clinical use of TMP was reported in 1962 and microbial resistance to TMP was identified by 1968 (25). There are three primary classes of resistance mechanisms. The first, largely used by gram-negative bacteria, are plasmid-encoded DHFR enzymes (34). The second, favored by gram-positive organisms, are point mutations. For example, TMP-resistant *Streptococcus pneumoniae* strains possess an Ile-to-Leu mutation at position 100 (39), while TMP-resistant *Staphylococcus aureus* strains contain a Phe-to-Tyr mutation at position 98 (23). These mechanisms are not mutually exclusive, and many plasmid-encoded DHFRs contain analogous point mutations, allowing escape from TMP action, as well as increasing the total DHFR. However, these resistance-conferring mutations compromise enzymatic function (23, 39).

The third mechanism of TMP resistance is a poorly understood intrinsic property of the chromosomally encoded DHFR (4). This class includes the gram-positive organism *B. anthracis* (6), as well as *Mycobacterium* species (8). One proposal is that selectivity arises from the volume of the binding site (16, 49). This is directly related to TMP resistance and generally correlates with more favorable K_m values for FAH_2 (3, 12, 39, 45), thus making it harder to displace. However, exceptions that are TMP sensitive with a low K_m for FAH_2 do exist, such as *Lactobacillus casei* (24). Previous work has also highlighted single amino acid changes relative to susceptible organisms to explain innate resistance. In particular, *B. anthracis* codes for Tyr at position 102 (equivalent to *S. aureus* position 98). However, crystallographic evidence has shown that this residue is distant from the active site (10). A previous crystal structure of *B. anthracis* DHFR attributed TMP resistance to residue Phe96, which is an Ile in TMP sensitive organisms, and presented modeling studies that indicated its involvement in TMP resistance via steric mechanisms (10).

We have previously identified dihydrophthalazine TMP derivative inhibitors for this target (7). Variation of the moiety

* Corresponding authors. Mailing address for C. R. Bourne: Department of Veterinary Pathobiology, 250 McElroy Hall, Oklahoma State University, Stillwater, OK 74078. Phone: (405) 744-5275. Fax: (405) 744-6736. E-mail: christina.bourne@okstate.edu. Mailing address for W. W. Barrow: Department of Veterinary Pathobiology, 250 McElroy Hall, Oklahoma State University, Stillwater, OK 74078. Phone: (405) 744-1842. Fax: (405) 744-3738. E-mail: bill.barrow@okstate.edu.

† Supplemental material for this article may be found at http://aac.asm.org/.

▽ Published ahead of print on 13 April 2009.

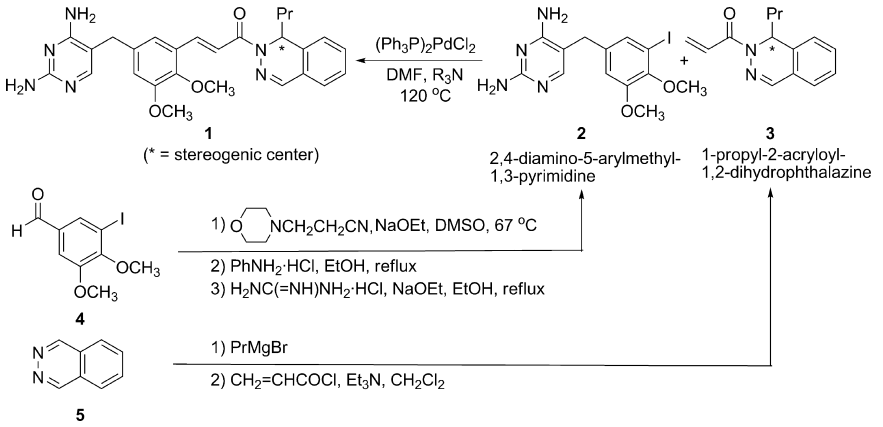

FIG. 1. Chemical synthesis of RAB1.

attached to the dihydrophthalazine ring produced 50% inhibitory concentrations (IC_{50}s) ranging from 46 to 600 nM (6). In the same assay, an IC_{50} of 15 nM for the universal DHFR inhibitor MTX was obtained, while that for TMP was 77 mM (5). Among the most effective of the dihydrophthalazine-based inhibitors is BAL17662, now referred to as RAB1, with an MIC of $\leq$12.8 μg/ml and an IC_{50} of 54 nM. In the present study, we cocrystallized RAB1, (*S*,*E*)-3-(5-((2,4-diaminopyrimidin-5-yl) methyl)-2,3-dimethoxyphenyl)-1-(1-propylphthalazin-2(1*H*)-yl)prop-2-en-1-one, with *B. anthracis* DHFR and report the structure to a 2.3-Å resolution. We have also obtained a crystal structure of *B. anthracis* DHFR complexed with TMP, although a crystal lattice defect, termed pseudomerohedral twinning, has limited our interpretation of these data. These structures provide insight into the success of this compound over the parent TMP molecule and highlight previously unappreciated areas of the binding site that are critical for selective inhibition of this enzyme.

(Portions of this study were presented as a poster at the conference "Understanding and Controlling Infectious Diseases: an Agenda for the 21st Century" at the Institute Pasteur, Paris, France, on 11 to 13 November 2008.)

MATERIALS AND METHODS

Chemical synthesis of RAB1. The synthesis of RAB1 was carried out using a Heck reaction for the coupling of compounds 2 and 3 (Fig. 1). Diaminobenzylpyrimidine (compound 2) was prepared from 5-iodo-3,4-dimethoxybenzaldehyde (compound 4) (41) by base-promoted condensation with 3-morpholinopropionitrile (50), followed by treatment with guanidine hydrochloride and sodium methoxide (47) (Fig. 1). Dihydrophthalazine (compound 3) was prepared by the addition of propylmagnesium bromide to phthalazine (compound 5), followed by acylation of the addition product with acryloyl chloride (30, 31) (Fig. 1).

The building block compounds 2 and 3 were generated on a large scale in 50 to 60% yields. The original work (30, 31) cited yields for the Heck coupling in the 15 to 30% range on gram-scale reactions. In a preliminary experiment, a yield of nearly 40% was obtained by using $(Ph_3P)_2PdCl_2$ as the catalyst and 1-ethylpiperidine as the base in dimethylformamide at 120°C for 24 h (Fig. 1). Detailed chemical synthesis is given as part of the supplementary information. Synthesized RAB1 was evaluated as previously published and has the same MIC against *B. anthracis* Ames as initially reported, i.e., between 8 and 16 μg/ml (7).

Protein purification and crystallization. Expression of recombinant *B. anthracis* DHFR was achieved by using a published protocol (6). Purification proceeded as previously described using HisTrap format immobilized metal affinity chromatography resin (GE Healthcare). The His tag was cleaved by using a Novagen thrombin cleavage kit, leaving four additional nonnative C-terminal residues (Leu, Val, Pro, and Arg). Final purification utilized a HiPrep 26/60 Sephacryl S-100 size exclusion column. All stages of purification were monitored by sodium dodecyl sulfate–12.5% polyacrylamide gel electrophoresis and resulted in purification of >98%. Protein concentrations were calculated based on A_{280} values using ε280 of 1.22 (calculated by ExPASy [29]).

Protein samples were concentrated to ~5 optical density units/ml, and a 10× molar excess of solid ligand was added to the solution, followed by gentle mixing to aid dissolution. The protein-ligand mixture was further concentrated and crystallization trials were initiated. The *B. anthracis* DHFR-RAB1 cocrystals grew within 1 to 2 days at 22°C in a sitting-drop format from a 30-mg/ml protein stock solution mixed 1:1 with a well solution of 12% PEG3350, 0.2 M $CaCl_2$, 0.1 M MES [2-(*N*-morpholino)ethanesulfonic acid; pH 5.8], and 3% glycerol. The *B. anthracis* DHFR-TMP cocrystals grew within 10 days at 22°C in a sitting-drop format from a 42.5-mg/ml protein stock solution mixed 1:1 with a well solution of 13% PEG3350, 0.2 M $CaCl_2$, 0.1 M MES (pH 5.45), and 1% ethanol.

X-ray data collection, processing, and structure quality. The best X-ray diffraction data were collected from single crystals that were cryoprotected with a 50:50 mixture of Paratone-N and paraffin oil and then vitrified by plunging them into liquid nitrogen. The data were collected on a Bruker Microstar/X8 Proteum with a Cu rotating anode (λ = 1.54 Å) equipped with Montel multilayer optics and operated at 45 kV and 55 mA. The crystal temperature was maintained with an Oxford Cyrostream COBRA low temperature, self-generating nitrogen device.

X-ray data were indexed and integrated with Saint, scaled with SADABS, and merged with XPREP (14); pertinent statistics are presented in Table 1. A molecular replacement solution in the space group $P2_12_12_1$ and containing eight molecules per asymmetric unit was readily determined with Phaser through CCP4 (15) using a published *B. anthracis* DHFR structure (Protein Data Bank [PDB] ID code 2QK8) (10) as the search model (with water and MTX removed). Initial maps using unrefined phases revealed well-defined main-chain and side-chain electron density throughout each molecule, including the four extra C-terminal residues remaining from tag cleavage and RAB1 molecules (see Fig. S1 in the supplemental material). Refinement was carried out with PHENIX (1) and included restraints based on eightfold noncrystallographic symmetry. The RAB1 model was built using a SMILES string notation with the Elbow module of PHENIX. Manual rebuilding was carried out with the program Coot (27).

Data for the +TMP cocrystal were processed in space group P1 and evaluated for correct assignment with XPREP (14), which indicated space group P121 as the most likely. However, data could be processed equally well in space groups $P222_1$ or $P4_1$. In all cases twinning, with coordinates (h, -k, -l), was identified. This defect arises from specific crystal packing contacts and makes the computational aspect of structure determination more error-prone, causing the resulting electron density to be less clear. In the case of +RAB1 many such twinned crystals were also obtained; however, a different crystal form ($P2_12_12_1$) was identified. The lowest final R factors were obtained in space group P2 with eight molecules per asymmetric unit. Since maximum-likelihood refinement is not available with twinning, a least-squares target was used for refinement with PHENIX (1). The twin law "h, -k, -l" was included during refinement, which produced a twin fraction of 0.49. Model bias was evident within one to two macrocycles, particularly at the extended C termini (visible as in the +RAB1 structure). This bias results from the detwinning procedure's dependence on

TABLE 1. X-ray data collection and crystallographic refinement statistics

Data collection and refinement	+RAB1	+TMP[a]
Data collection		
Space group	$P2_12_12_1$	P2
Unit cell (Å, °)	68.2, 135.9, 168.7	67.9, 67.6, 167.0, β = 90.12
Resolution in Å (range)	25–2.3 (2.4–2.3)[b]	30–2.4 (2.5–2.4)
R_{sym}	0.123 (0.476)	0.088 (0.281)
I/σI	16.1 (4.8)	13.1 (4.9)
Completeness (%)	97.3 (96.7)	90.1 (72.5)
Redundancy	13.7 (11.2)	4.7 (2.7)
Refinement		
No. of reflections	69,571	53,699
R_{work}/R_{free}	0.206/0.250	0.237/0.309
No. of atoms		
Protein	10,800	10,663
Ligand/ions	288	176
Water	1,521	371
B factors (Å^2)		
Protein	28.9	31.1
Ligand/ions	35.7	32.3
Water	32.4	30.4
RMS deviations		
Bond length (Å)	0.007	0.004
Bond angle (°)	1.051	0.836

[a] The +TMP structure was refined with the (pseudomerohedral) twinning law (h, -k, -l) and resulted in a twinning fraction of 0.49.
[b] Values for the highest-resolution shell are indicated in parentheses.

the model (26) and significantly complicated refinement efforts. Although electron density for TMP was less clear in the maps from molecular replacement, application of twinning corrections (in the absence of TMP) during cycles of refinement produced unambiguous density (see Fig. S1 in the supplemental material).

The final structure complexed with RAB1 was refined to an R_{work} of 20.6% and an R_{free} of 25.0% (Table 1). A Ramachandran plot revealed 97.1% of residues in the favored region (1,299 total residues), 99.6% in the allowed region, and 0.4% (5 residues) in the nonfavored region of stereochemical space. Four of these five residues are located in a strained turn at amino acids 18 and 19, while the fifth is in a C terminus. Chain H is the most poorly defined, and loops 67 to 73 and loops 88 to 89 were removed. In addition, numerous side chains throughout all models were truncated to alanine as a result of high mobility, resulting in poorly defined electron density (listed in the supplemental material).

The final structure complexed with TMP was refined to an R_{work} of 23.7% and an R_{free} of 30.9% (Table 1). A Ramachandran plot revealed 90.8% of residues in the favored region (1,279 total residues), 98.4% in the allowed region, and 1.6% (21 residues) in the nonfavored region of stereochemical space. These residues lie in poorly defined regions, including the strained turn encompassing residues 17 to 19, Asn66, a flexible loop from residues 131 to 135, and the C termini of each chain. For each chain, at least one residue was removed from the loop at positions 131 to 135; the four C-terminal residues are not visible for chain B. As for the +RAB1 structure, numerous side chains were truncated to alanine as a result of high mobility, resulting in poorly defined electron density (listed in the supplemental material).

Calculations of binding energy for complexes of *B. anthracis* DHFR with RAB1 and TMP, as well as with the superposition of RAB1 into the human DHFR binding site, were carried out with APBS (5) using the Python molecular viewer (http://mgltools.scripps.edu/). Coordinates and structure factors have been deposited and given the codes 3FL8 for the complex with RAB1 and 3FL9 for the complex with TMP.

RESULTS

Structure of *B. anthracis* DHFR-RAB1 complex. The crystallographic repeating unit contained eight complexes in the asymmetric unit, each with a fully occupied RAB1. Despite cocrystallization with a racemic mixture, the crystal structure of RAB1 in the complex was found exclusively as the *S*-enantiomer (Fig. 2), which corresponds to the active enantiomer of MTX and follows the same path as the glutamate moiety of the *p*-aminobenzyl glutamate (pABG) tail (10). This selection seems controlled by the position of Arg53, since it is hydrogen bonded to the ligand, which then occupies the space needed to accommodate the other enantiomer if bound in the same overall conformation (Fig. 3A).

The 2,4-diaminopyrimidine moiety is situated in a conserved pocket and makes hydrogen bonds to Met6, Val7, Glu28, Phe96, Tyr102, and Thr115, as expected (Fig. 2). These interactions are similar to those observed in complexes of DHFR with the natural substrates FAH_2 (44), MTX (10), TMP (16, 38), and *B. anthracis* DHFR complexed with another TMP derivative (9). The dimethoxybenzyl moiety (a trimethoxybenzyl in TMP) is enclosed in a hydrophobic channel composed of residues Asn19, Asn20, Leu21, Asn47, Ala50, and Ile51 on one side and Leu29 on the other, with Phe96 contacting the underside (Fig. 2). The dimethoxybenzyl group is oriented to present the methoxy substituents to the more polar, solvent-exposed top of the binding site. The acryloyl linker region contains the only other hydrogen bond to protein, albeit among the weakest (3.73 Å), between the carbonyl oxygen of the linker and a terminal nitrogen from the guanidine group of Arg53 (Fig. 2). In six of the eight copies of the complex with RAB1, this hydrogen bond is supplemented by a water bridge between Arg53 and the linker carbonyl.

The dihydrophthalazine moiety is deeply embedded in a continuation of the hydrophobic channel, surrounded by residues Leu55 and Pro56 on one side and Leu29, Gln30, Val32, Lys33, Thr36, and Leu41 on the other and terminating with Arg58 (Fig. 2). In particular, the face of the dihydrophthalazine moiety contacts the aliphatic chain of Lys33 on one side and Leu55 on the other. Note that a critical component of this tight steric fit is the presence of only two double bonds in the proximal dihydropyridazine portion of the dihydrophthalazine ring, allowing this moiety to bend from planarity (Fig. 3B). The resulting angle ranges from 107° to 117°, depending on which of the eight copies is analyzed (noncrystallographic restraints were not applied to RAB1). The aliphatic portion of Arg58 delineates the end of the binding site, and it undergoes a substantial conformational change in the binding site as a result of RAB1 binding. The terminal guanidino group swings away from the site by 2.3 Å and toward solvent to allow the dihydrophthalazine moiety full access to the site (Fig. 3C). The movement of the Arg58 side chain is only possible with a concomitant movement of Met37 by 4.4 Å (at the base of helix A).

The loop centered on residue 18 is under strain as evidenced by outlying φ-ψ angles in the Ramachandran plot, poor electron density, and increased B factors. These residues contact NADPH (9) and shows less order in its absence. The construct used for the current structure retains four extra C-terminal residues after His tag cleavage (Leu, Val, Pro, and Arg) which are visible in the electron density map. This C-terminal tail plays an intricate role in crystal packing by inserting into a polar pocket composed of residues Arg45, Lys46, Arg65, and Gln100 from a neighboring molecule (see Fig. S2b in the supplemental material). In addition, one calcium ion per molecule

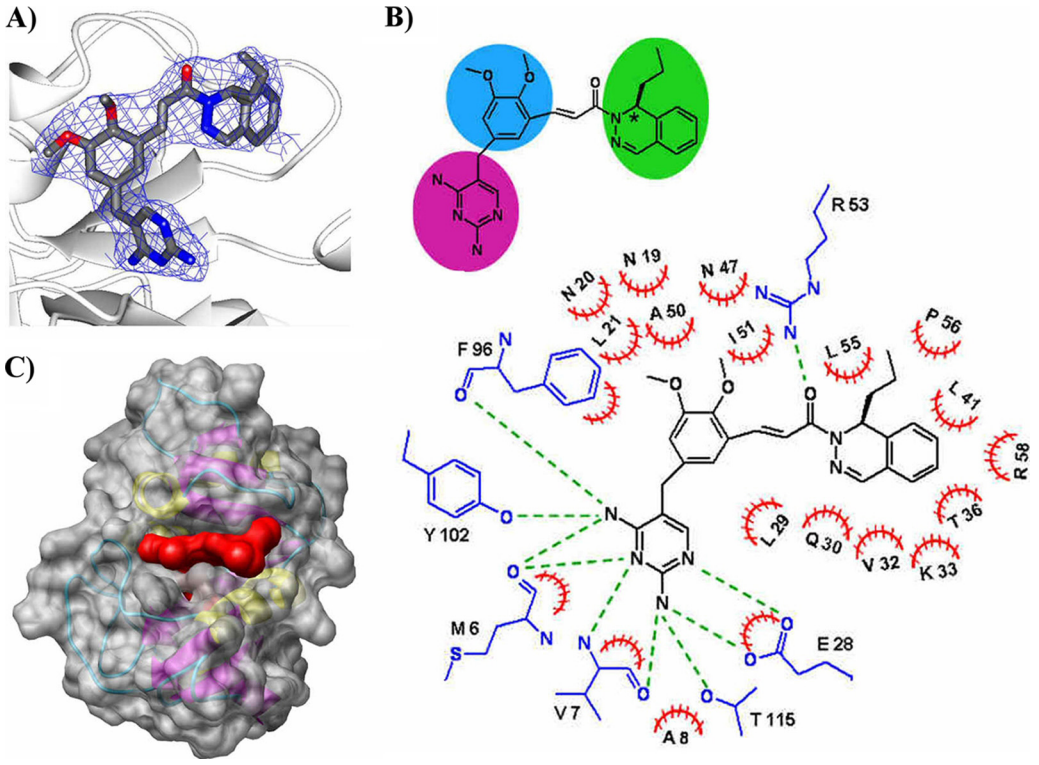

FIG. 2. The well-defined density for RAB1 highlights a fit to the binding site that is complementary in shape and composition. (A) Electron density from refinement prior to the addition of RAB1, contoured at 1σ. (B) RAB1 structure and plot of intermolecular contacts: magenta, 2,4-diaminopyrimidine group; blue, dimethoxybenzyl ring; green, dihydrophthalazine moiety. The acryloyl linker is uncolored; the enantiomeric carbon is denoted by an asterisk. Residues depicted in blue are involved in hydrogen bonds to RAB1, denoted by green dashed lines. Red hatched semicircles indicate hydrophobic interactions. (C) *B. anthracis* DHFR structure with the surface indicated in gray and RAB1 surface indicated in red. Both the N and C termini are obscured at the back of the molecule in this view.

was located and also bridges crystal contacts. This calcium ion is coordinated by Asp110 (monodentate), the mainchain carbonyl of Tyr108, three water molecules, and Gln147 (monodentate) from a neighboring DHFR molecule (see Fig. S2c in the supplemental material). One of the water molecules helps stabilize the conformation of the N terminus by forming a hydrogen bond with the main chain carbonyl of Met1. The C-terminal interactions are presumed responsible for the change in crystallographic space group and increased resolution compared to a previous structure with MTX (PDB ID code 2QK8) (10), while no conformational changes are noted resulting from calcium binding.

Comparison of *B. anthracis* DHFR-RAB1 and *B. anthracis* DHFR-TMP structures. As part of the present study, a structure of *B. anthracis* DHFR cocrystallized with TMP has also been obtained. In this case, intermolecular contacts favored packing in space group P2 and, unfortunately, this crystal is a

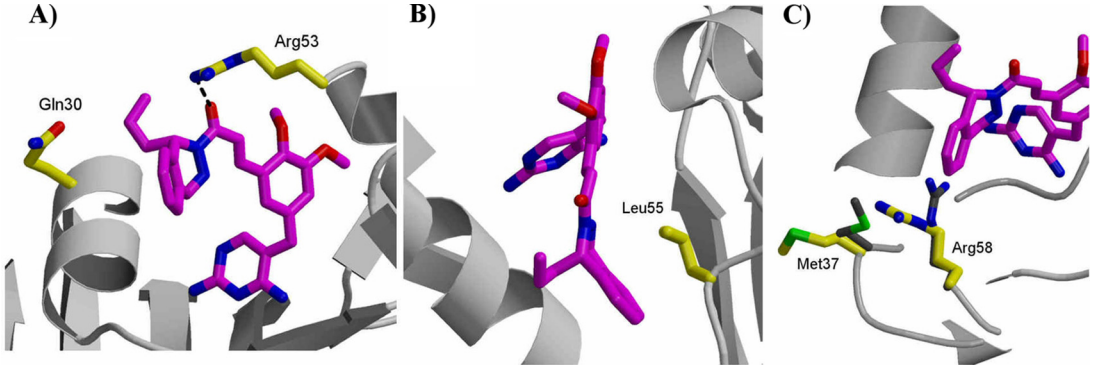

FIG. 3. Key interactions modulate the conformation between *B. anthracis* DHFR and RAB1. (A) The side chain of Arg53 would sterically interfere with binding of the opposite enantiomer; only the *S*-enantiomer of RAB1 can be accommodated. (B) The side chain of Leu55 conforms to the observed bend in the dihydropyridazine ring of RAB1's dihydrophthalazine moiety. (C) The side chains of Arg58 and Met37 undergo a conformational change (indicated from gray to yellow) to accommodate the dihydrophthalazine moiety of RAB1.

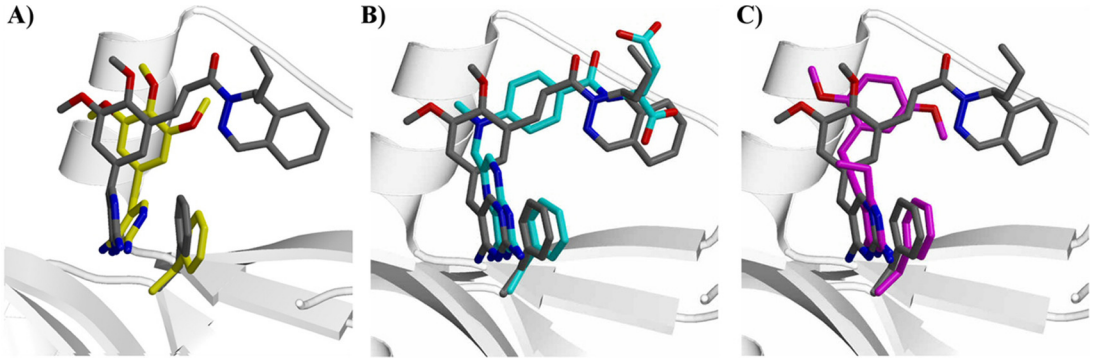

FIG. 4. Superposition of ligands with RAB1 (gray) reveals minor shifts in Phe96 and otherwise conserved binding site architecture reflected by the similarity of ligand conformation. (A) TMP (yellow); (B) MTX (cyan); (C) C17 (magenta).

perfect pseudomerohedral twin (Table 1). Notwithstanding crystallographic limitations, this structure demonstrates that *B. anthracis* DHFR can bind to TMP despite the organism's innate resistance (IC_{50} = 77.2 mM), which has been demonstrated to result from the chromosomally encoded DHFR used in these studies (6). However, it must not bind as well as the natural substrate, FAH_2, since it is not a successful competitive inhibitor for the enzyme (5). This is similar to the structure of *M. tuberculosis* DHFR (38) complexed with TMP, indicating that successful cocrystallization does not necessarily correlate with productive in vivo inhibition.

Sequence alignment of TMP-sensitive and TMP-resistant organisms highlighted position 96 as possibly involved in overcoming TMP inhibition; sensitive organisms contain Ile, while *B. anthracis* contains Phe (10). As shown in the structure, TMP is accommodated within the *B. anthracis* DHFR binding site (Fig. 4A). The closest contact between TMP and Phe96 is just over 3 Å. When superposed with the RAB1 structure, itself a TMP derivative, it is evident that the dimethoxybenzyl ring shifts significantly (1.1- to 1.8-Å translation, with the diaminopyrimidine ring tilted ~35°) to accommodate the longer ligand structure of RAB1. Thus, Phe96 does appear to provide a pivot point for the ligand motion, differing from the +RAB1 structure by 0.9 Å and tilting ~30° (Fig. 4A). There are no other substantial changes in the enzyme conformation when the +RAB1 and +TMP structures are compared aside from the conformational change of Arg58 and Met37 in the presence of RAB1. The binding site appears somewhat more hydrated when TMP is bound instead of RAB1, including a buried water coordinated between a methoxy group of TMP and Asn46 and a transient water in the binding site coordinated with Arg58. Although Phe96 is not an impediment to binding, it and neighboring Gly97 are under strain, as evidenced by movement and the unusual rotameric configuration at Phe96. The linker region and the dihydrophthalazine moiety of RAB1 more than double the binding surface relative to TMP. This size increase, combined with favorable steric constraints and compatible hydrophobicity, significantly increases the binding affinity and accounts for the successful inhibition of *B. anthracis* with TMP-derived RAB1.

Comparison of *B. anthracis* DHFR-RAB1, DHFR-MTX, and DHFR-C17 complexed structures. Prior to this structure determination, there were two available *B. anthracis* DHFR crystal structures: one complexed with MTX (9) and the other complexed with a TMP-derived propargyl inhibitor referred to as compound 17 (C17) (8). The binding site of DHFR enzymes is considered to be relatively rigid (38), and this is highlighted by the very close superposition of enzyme-bound RAB1, MTX (10), and C17 (9) (Fig. 4). RAB1 possesses the most surface area for interaction (~690 $Å^2$ buried versus MTX ~590 $Å^2$ buried versus C17 ~510 $Å^2$, calculated with LPC software [45]) and greater torsional freedom resulting from the diaminopyrimidine versus MTX and the diaminopteridine of FAH_2, as well as a more flexible acryloyl linker beyond the diaminopyrimidine versus C17's stiff propargyl linkage. This allows RAB1 to more easily conform to the binding site. Ligand flexibility has previously been touted as a predictor of selectivity (17).

The conformations of *B. anthracis* DHFR are very similar in all determined complexes. Comparison of the +RAB1 structure to these complexes gives rise to an root mean square (RMS) deviation at the α-carbon atoms ranging from 0.46 to 0.62 $Å^2$ (9). Among the larger differences is the gain of a helix from residues 132 to 134 connecting β-strand F to β-strand G (see Fig. S2a in the supplemental material) in the +RAB1 and +C17 complexes (9). In the +MTX and +TMP complexes, this region is a flexible loop, causing it to maintain a random conformation with a >2-$Å^2$ RMS deviation from the current structure. However, this region is distant from the binding site and is not expected to affect enzymatic function.

While the position of the protein chains comprising the binding sites are relatively invariant, analysis of their flexibility through use of crystallographic B factors reveal ligand-dependent stresses (where higher B factors indicate more flexibility). The loop on one side of the site extends from residues 20 to 33, partially encompassing helix A, and is believed to contain regulatory elements for binding in some bacterial species (19, 44). The largest differences are seen at residues 21 to 25, with shifts in the main chain conformation of >1 Å relative to the MTX complex (see Fig. S3a in the supplemental material), resulting in a narrowing of the MTX-complexed binding site. This conformational shift is, in part, caused by an interaction of Leu21 with the face of the dimethoxybenzyl in +RAB1 and +C17, which is much weaker in +MTX due to the placement of the benzyl ring further from this residue. Another major contributor to this ordering is a crystal packing contact between Arg24 and Asn89 of a neighboring molecule in the +RAB1 complex

(see Fig. S2d in the supplemental material) and a similar contact in the +C17 complex between Arg24 and Glu67 of a neighboring molecule. This culminates in an ordering of this region for +RAB1 and +C17 complexes, exemplified by the average B factors for residues 21 to 25: +RAB1 is 27.5 ± 1.4 Å^2 and +C17 is 22.8 ± 2.1 Å^2, while +MTX is considerably higher at 65.3 Å^2 (see Fig. S3b in the supplemental material).

The other side of the binding site is composed of residues 50 to 58, and this loop is shifted outward from the site by a modest 0.5 to 0.7 Å when RAB1 is present (see Fig. S3a in the supplemental material) and a more dramatic >1 Å outward when C17 is present. Previous estimates claim this movement correlates with potency (9) and, in a crude approximation, it does appear that the binding site is more closed at this position as affinity increases. This is centered on residues 50 to 51, which are adjacent to the dimethoxybenzyl ring of RAB1 and the 5′-methoxy group of C17. In the +C17 complex, this region is also stabilized by interaction of NADPH with helix B (residues 45 to 52). These trends are evident in B factors of 53.3 ± 3.9 Å^2 with +RAB1 and 36.3 Å^2 with +MTX, while they are only 27.1 ± 0.1 Å^2 with +C17 (see Fig. S3b in the supplemental material). However, the lack of extensive ligand contacts with +C17 causes this conformational change to propagate to residue 54, making the binding site in the presence of C17 wider overall. It is presumed that it is precisely these ligand contacts with RAB1 that impart larger B factors in this region as both ligand and protein adjust to fit to one another.

Despite these differences, superposition of the RAB1-, C17-, and MTX-complexed structures reveals a striking similarity in ligand position (Fig. 4). It is expected that the diamino moieties would occupy the same space, but the position differs slightly for RAB1. The maximal translation is ~0.5 Å seen around the 1′ position, and the ring is tilted, pivoting from the 4′-amino group, by almost 20°. This positioning is due to steric restrictions of fitting the dihydrophthalazine moiety in the other end of the site, causing the entire ligand to shift toward the end of the binding site occupied by the diamino ring and thus the NADPH site. This results in a more favorable hydrogen bond to the Tyr102 side chain but also imposes some possible steric constraints with the NADPH molecule. Since this was not present in the +RAB1 complex, the +C17 complex was superposed and clashes between the NADPH and RAB1 were visualized. In particular, the linker between the 2,4-diaminopyrimidine ring and the dimethoxybenzyl is only 2.4 Å from the nicotinamide ring of NADPH. In addition, the 3′-methoxy group is only 2.3 Å from the ribose ring of the nicotinamide moiety. It is possible that minor adjustments of binding positions could relieve these close proximities if both NADPH and RAB1 were present in the same molecule. The other structural differences in ligands at this position arise from the presence of an additional ethyl group attached to C17's 2,4-diaminopyrimidine ring at position C6, which allows C17 to more closely approach Trp23 and Leu21. Although the identities of the small molecule structures diverge past the 2,4-diaminopyrinidine ring, they follow the same path through the binding site. Not surprisingly, the contact residues are also quite similar.

Among differences in the binding of these ligands, the hydrogen bond between the ligand and Arg53 is variable. It is relatively weak with RAB1 (3.73 Å), is much stronger with the carbonyl from the pABG group of MTX (2.80 Å) (10), and is absent in C17 due to lack of a hydrogen acceptor for interaction (9). Numerous differences exist due to the smaller size of C17, such as the Lys33 side chain, which folds over and partially obstructs the downstream binding pocket. Adjacent to this is Gln30, which mirrors the pABG Glu of MTX or the propyl group of RAB1, but has no contacts with C17, and the rotamer is positioned away from the binding site. In addition, C17 does not contact Pro56 or Arg53, whereas the other two ligands do. Overall, the number of hydrogen bonds qualitatively follows the affinity for these ligands, with 14 hydrogen bonds to MTX, 10 to RAB1, and 9 to C17. It is noteworthy that the methoxy groups of RAB1 and C17 do not contribute to the hydrogen bonding pattern of either molecule.

Some interactions are unique to RAB1 due, in part, to the bulk of the buried dihydrophthalazine moiety. Thr36 and Leu41 line the bottom of the site and contact the base of the dihydrophthalazine group on opposite sides (Fig. 2). The conformation of Arg58 is the same in the +C17 and +MTX complexes, confirming that the conformational change in the presence of RAB1 is due to steric requirements. This is also true at Met37, which shifts at the α-carbon by 0.6Å away from the site when RAB1 is present. Leu55 in the +RAB1 complex is found in a different rotameric configuration, which is consistent with its role in the steric fit of the dihydrophthalazine moiety of RAB1 (Fig. 3B). Of relevance to TMP resistance, Phe96 shifts by 0.4 to 0.6 Å with RAB1 versus +MTX or +C17 (Fig. 4), probably to maintain favorable van der Waals interactions as the conformation of the 2,4-diaminopyrimidine ring is altered.

How is RAB1 selective against the human DHFR enzyme? Previous studies revealed a high selectivity of RAB1 for *B. anthracis* DHFR over human DHFR (IC_{50} = 54 nM versus 110,000 nM) (7). A comparison of binding sites was made using the human DHFR structure complexed with MTX and NADPH (PDB ID code 1U72, RMS deviation = 2.05 Å) (20). Ligands were removed, and RAB1 was placed by superposition; putative clashes were identified with the aid of the Ligand Protein Contacts server (46).

Previous investigations have identified human Phe31, equivalent to *B. anthracis* residue Leu29 and human residue Pro61 (inserted relative to *B. anthracis*), as key residues responsible for the lack of selectivity for the human DHFR enzyme (9, 10). In RAB1 these residues are closest to the acryloyl linker region. Human Phe31 may impose minor restrictions that are expected to be accommodated by slight shifts in side chains and the flexibility conferred by the acryloyl linker of RAB1. The insertion containing hPro61 protrudes above the binding site and is situated well above the RAB1 superposed molecule, although it may impact the moiety at the stereocenter (see below). However, this loop may affect the accessibility of the site, particularly since it is opposite human Phe31. These dynamics of accessibility would not be discernible from available crystal structures.

Human Phe34, equivalent to *B. anthracis* Val32, is found at the base of the binding site and would prevent RAB1 from seating as deeply within the pocket by impinging on the dihydrophthalazine moiety (Fig. 5A). Human Asn64, which is an insertion relative to *B. anthracis* but would be found between residues 52 and 53, collides with the stereogenic carbon and

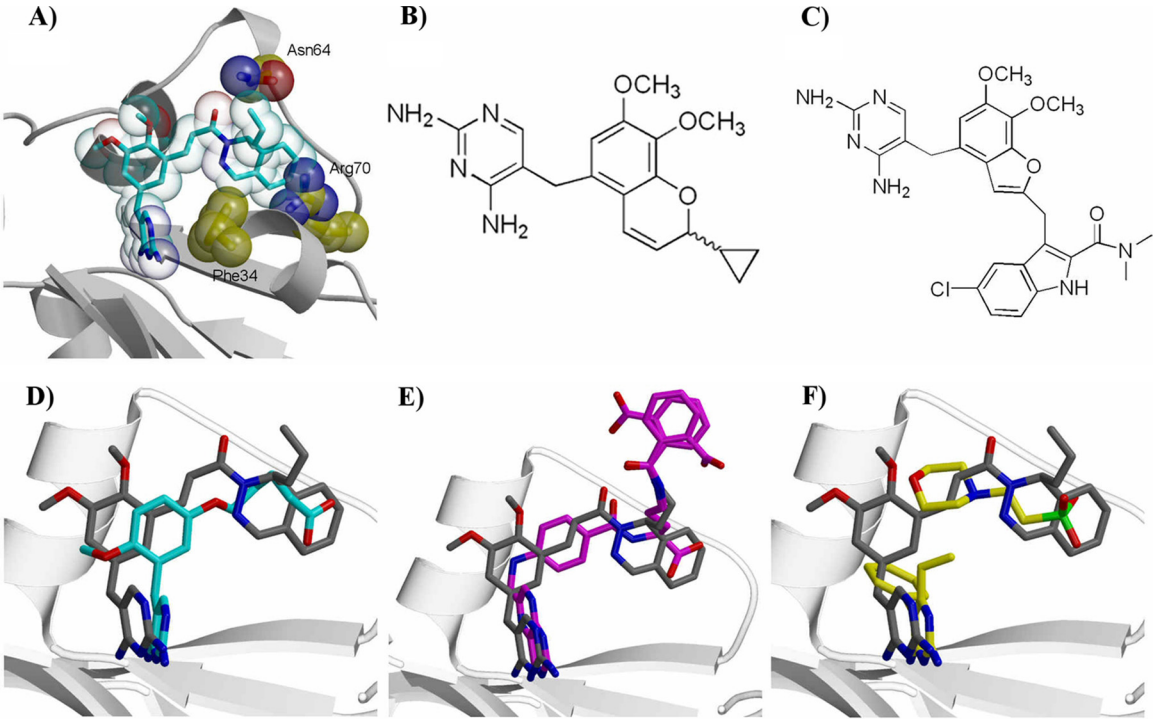

FIG. 5. RAB1 cannot fit in the human DHFR binding site due to steric clashes, and no other inhibitors with structural data possess the same determinants. (A) Human DHFR (PDB ID code 1OHJ [18]) with RAB1 (van der Waals surface shown) superpositioned into the binding site. Human residues Phe34, Asn64, and Arg70 are shown as van der Waals spheres. (B and C) Two-dimensional structures of Iclaprim (B) and AR-709 (C). (D to F) Superposition of RAB1 (gray) with 5-[ω-carboxy(alkyloxy)] TMP derivatives (cyan, PDB ID code 2FZH) (21) (D); PT523, also a TMP derivative (magenta, PDB ID code 1OHJ) (18) (E); and pyrimethamine (yellow, PDB ID code 2BLB) (37) (F). A fortuitous buffer molecule (MES) is in a position roughly equivalent with the acryloyl linker-dihydrophthalazine moiety of RAB1. This indicates unfilled binding site volume in the presence of pyrimethamine, allowing the buffer molecule room to bind, that in turn is filled by RAB1.

propyl group extension. The largest steric clash is found with human Arg70 and the dihydrophthalazine moiety, equivalent to *B. anthracis* Arg58, which undergoes a conformational change to relieve a similar issue of close proximity (Fig. 5A). However, the human enzyme contains an inserted loop (residues 41 to 47) that would limit the area available to human Arg70 for this conformational change. This is likely a key difference that significantly contributes to the observed selectivity. It is unlikely that a cocrystal could be obtained between human DHFR and RAB1 due to these steric clashes. These results strongly suggest that the dihydrophthalazine moiety is responsible for the selectivity of this entire class of diaminopyrimidine inhibitors (7).

DISCUSSION

RAB1 (previously BALB17662) contains a propyl group with a stereogenic carbon, and this system displayed the most favorable MIC and binding properties. Although membrane penetration clearly has a role in the selection of the best inhibitor, a shorter ethyl or longer butyl group at this position did not perform as well in IC_{50} measurements (96 and 170 nM, respectively) (7). The propyl group protrudes upward from the binding site and terminates at the transition to solvent. It is likely that shorter chains provided slightly less surface area for binding, while longer chains caused stress by exposure to the solvent. However, the IC_{50} for RAB1 (54 nM) is still above that of MTX (12.2 nM) (6). This is likely a result of the loss of the polar pABG group, which provided an additional four hydrogen bonds. Minimal efforts have been made to incorporate polar adducts in similar positions within the current series of inhibitors, but such will be considered in future refinements.

The PDB (11) contains well over 100 DHFR structures from various species, and many of these are complexes with inhibitory small molecules. An attempt was made to compare the size of these ligands with RAB1. Among the larger inhibitors identified were two 5-[ω-carboxy(alkyloxy)] TMP derivatives complexed with *P. carinii* (PDB ID codes 2FZH and 2FZI) (21), as well as the inhibitor PT523, also a TMP derivative, complexed with human DHFR (PDB ID code 1OHJ) (18) (Fig. 5D and E). However, their molecular extensions beyond the diaminopyrimidine are aliphatic in composition, and the termini are capped with a polar carboxylic acid, such as is found in MTX. Many MTX derivatives have been described that also seem to trend toward extended aliphatic extensions, but these compounds lack structural data for direct three-dimensional comparison (36, 42, 43). Interestingly, some *Plasmodium* and *Candida* structures, which are considerably different from the *B. anthracis* enzyme, contain inhibitors, as well as a fortuitous buffer molecule (MES) in a position roughly equivalent with the linker-dihydrophthalazine portion of RAB1 (PDB ID code 2BLB) (37, 48) (Fig. 5F), indicating unoccupied volume within the binding site complexed with those inhibitors. These are all in direct contrast to the large

hydrophobic bulk of the dihydrophthalazine moiety that is the basis for this series of TMP-derived inhibitors (7), which confers both affinity and selectivity at the structural level. This indicates that the DHFR binding site, in general, can accommodate larger inhibitory ligands than has previously been appreciated.

It is striking that the conformation of the TMP-derived RAB1 is so similar to that of MTX and yet, unlike MTX, RAB1 does not inhibit human DHFR. The similarity of conformation is directly attributable to the rigidity of the DHFR binding site (Fig. 4C). The dihydrophthalazine moiety is responsible for the lack of selectivity for the human enzyme that is observed with this class of inhibitors (Fig. 5A) (7). Although accommodation of RAB1 required a conformational change, this was limited to the side chains of Arg58 and, in turn, residue Met37, highlighting the limited plasticity of this site (Fig. 3C). A class of *P. carinii* carboxyalkyloxy inhibitors identified an obstruction of Arg70 (equivalent to *B. anthracis* Arg58), and cocrystallization trials failed to observe either ligand or that end of the ligand (22), due presumably to steric interference from the Arg side chain. However, the dihydrophthalazine moiety of RAB1 is capable of swinging the equivalent Arg side chain out of the way. This is likely an effect of affinity, where the free energy of binding is low enough (i.e., high affinity) to offset the energetic consequence of a conformational change and is reflected by a modest 1.5 cal/mol binding energy. This is in contrast to the negative binding energies calculated for complexes with TMP (−5.0 cal/mol) and human DHFR with RAB1 (−9.2 cal/mol), indicating unfavorable interactions. The lack of other significant conformational changes in *B. anthracis* DHFR, while still accommodating the large hydrophobic dihydrophthalazine moiety, indicates the previously incomplete utilization of both the depth and the breadth of the DHFR binding site.

Development of new DHFR-specific inhibitors has been slow, despite being a highly validated target (33). The *B. anthracis* specific dihydropterin reductase inhibitor MANIC is reported to inhibit *B. anthracis* DHFR, although the IC_{50} is higher than that for TMP (102 μM [10] versus 77 μM [6]). The recent structure of *B. anthracis* DHFR complexed with C17 (9), as discussed above, highlights the vulnerability of this organism by targeting its DHFR enzyme. However, C17 and related inhibitors are still preliminary and, as such, possess IC_{50}s only in the micromolar range and have poor selectivity versus human DHFR. Both MANIC and C17 are smaller ligands than RAB1, again emphasizing the role of the larger structure in providing affinity and specificity. This is apparent compared to +TMP, which does present some strain around residue Phe96 but is still accommodated within the binding site. It is unclear from structural work why TMP is not an effective in vivo inhibitor of *B. anthracis* DHFR, although it seems unlikely to be a simple point mutation(s). More likely, the lack of inhibition is due to an intrinsic property of binding site dynamics and is probably similar to the as-yet-unknown reason behind a lack of inhibition of the human enzyme.

Arpida, a Swiss-based company, currently has at least two DHFR inhibitors: Iclaprim in phase III trials and AR-709 in late preclinical development (32). Iclaprim is noted to be broad spectrum and can also target TMP-resistant organisms (Fig. 5B). They surmise from modeling studies that resistance is overcome due to unique contacts with residues Ile50 and Leu54 (*B. anthracis* Ile51 and Leu55) (32). It is of note that both of these residues are involved in RAB1 binding (but not TMP binding) and, in particular, that Leu55 is responsible for the nonplanar conformation of the dihydropyridazine within the dihydrophthalazine moiety (Fig. 3B).

The other broad spectrum Arpida inhibitor under development, AR-709, is comparable in size to RAB1 and contains a terminal indole moiety substituted by a carboxamide group and a chlorine atom (Fig. 5C). Previous work sought to model the conformation of AR-709 based on the MTX complex (10) and, interestingly, seems to place the terminal indole along the top of the binding pocket (see Fig. 5C) (10). In light of the present complexed structure with RAB1, it is expected that the terminal indole would embed within the site much like the dihydrophthalazine moiety. The carboxamide group is modeled to protrude up and out of the site similar to the propyl group of RAB1. However, the carboxamide is considerably larger and, as modeled, presents a steric clash with the human DHFR residue Pro61. Other inhibitors in the same series as RAB1 contain benzyl, cyclopentyl, and cyclohexyl rings in place of the propyl group (7). It is likely that the binding modes would be similar to that of AR-709, although their performance was not as favorable as RAB1.

It is not a coincidence that larger DHFR inhibitors are being developed since the binding site can accommodate ligands larger than FAH_2, as seen here with RAB1. This additional bulk confers selectivity over the human enzyme and requires a minimal conformational change within the bacterial binding site. This approach is in contrast to previous suggestions that inhibitors should be no larger than the natural substrate to minimize resistance-conferring point mutations (37). Such a strategy would not provide the selectivity needed for a successful therapeutic. Future developments should follow the RAB1 backbone but also consider properties of solubility, bioavailability, and spectrum of activity. In particular, testing of more polar groups at the enantiomeric carbon will more fully explore additional hydrogen bonding potential analogous to MTX. We provide here the structural foundation for these explorations and validate *B. anthracis* DHFR as a viable and potent antibacterial target in the fight against infections.

ACKNOWLEDGMENTS

This study was supported by the Sitlington Endowed Chair in Infectious Disease to W.W.B.

We thank Basilea Pharmaceutica for collaboration during the preliminary stages of this project and Stacy Benson for maintenance of the Oklahoma State University X-ray Crystallography Facility.

REFERENCES

1. **Adams, P. D., K. Gopal, R. W. Grosse-Kunstleve, L. W. Hung, T. R. Ioerger, A. J. McCoy, N. W. Moriarty, R. K. Pai, R. J. Read, T. D. Romo, J. C. Sacchettini, N. K. Sauter, L. C. Storoni, and T. C. Terwilliger.** 2004. Recent developments in the PHENIX software for automated crystallographic structure determination. J. Sync. Rad. **11:**53–55.
2. **Adane, L., and P. V. Bharatam.** 2008. Modelling and informatics in the analysis of *P. falciparum* DHFR enzyme inhibitors. Curr. Med. Chem. **15:** 1552–1569.
3. **Appleman, J. R., W. A. Beard, T. J. Delcamp, N. J. Prendergast, J. H. Freisheim, and R. L. Blakley.** 1990. Unusual transient- and steady-state kinetic behavior is predicted by the kinetic scheme operational for recombinant human dihydrofolate reductase. J. Biol. Chem. **265:**2740–2748.
4. **Baccanari, D. P., and L. F. Kuyper.** 1993. Basis of selectivity of antibacterial diaminopyrimidines. J. Chemother. **5:**393–399.

5. **Baker, N. A., D. Sept, S. Joseph, M. J. Holst, and J. A. McCammon.** 2001. Electrostatics of nanosystems: application to microtubules and the ribosome. Proc. Natl. Acad. Sci. USA **98:**10037–10041.
6. **Barrow, E. W., P. C. Bourne, and W. W. Barrow.** 2004. Functional cloning of *Bacillus anthracis* DHFR and confirmation of natural resistance to trimethoprim. Antimicrob. Agents Chemother. **48:**4643–4649.
7. **Barrow, E. W., J. Dreier, S. Reinelt, P. C. Bourne, and W. W. Barrow.** 2007. In vitro efficacy of new antifolates against trimethoprim-resistant *Bacillus anthracis*. Antimicrob. Agents Chemother. **51:**4447–4452.
8. **Barrow, E. W., W. J. Suling, L. E. Seitz, R. C. Reynolds, and W. W. Barrow.** 2006. New antifolate inhibitors for *Mycobacterium avium*. Med. Chem. **2:**505–510.
9. **Beierlein, J. M., K. M. Frey, D. B. Bolstad, P. M. Pelphrey, T. M. Joska, A. E. Smith, N. D. Priestley, D. L. Wright, and A. C. Anderson.** 2008. Synthetic and crystallographic studies of a new inhibitor series targeting *Bacillus anthracis* dihydrofolate reductase. J. Med. Chem. **51:**7532–7540.
10. **Bennett, B. C., H. Xu, R. F. Simmerman, R. E. Lee, and C. G. Dealwis.** 2007. Crystal structure of the anthrax drug target, *Bacillus anthracis* dihydrofolate reductase. J. Med. Chem. **50:**4374–4381.
11. **Berman, H. M., J. Westbrook, Z. Feng, G. Gilliland, T. N. Bhat, H. Weissig, I. N. Shindyalov, and P. E. Bourne.** 2000. The Protein Data Bank. Nucleic Acids Res. **28:**235–242.
12. **Bock, R. A., J. L. Soulages, and W. W. Barrow.** 2007. Substrate and inhibitor specificity of *Mycobacterium avium* dihydrofolate reductase. FEBS J. **274:** 3286–3298.
13. **Bowden, K., N. V. Harris, and C. A. Watson.** 1993. Structure-activity relationships of dihydrofolate reductase inhibitors. J. Chemother. **5:**377–388.
14. **Bruker.** 2006. Proteum 2 Software Suite. Bruker AXS, Inc., Madison, WI.
15. **Collaborative Computational Project.** 1994. Collaborative computational project, number 4: the CCP4 suite: programs for protein crystallography. Acta Crystallogr. **D50:**760–763.
16. **Champness, J. N., A. Achari, S. P. Ballantine, P. K. Bryant, C. J. Delves, and D. K. Stammers.** 1994. The structure of *Pneumocystis carinii* dihydrofolate reductase to 1.9 Å resolution. Structure **2:**915–924.
17. **Cody, V., D. Chan, N. Galitsky, D. Rak, J. R. Luft, W. Pangborn, S. F. Queener, C. A. Laughton, and M. F. Stevens.** 2000. Structural studies on bioactive compounds. 30. Crystal structure and molecular modeling studies on the *Pneumocystis carinii* dihydrofolate reductase cofactor complex with TAB, a highly selective antifolate. Biochemistry **39:**3556–3564.
18. **Cody, V., N. Galitsky, J. R. Luft, W. Pangborn, A. Rosowsky, and R. L. Blakley.** 1997. Comparison of two independent crystal structures of human dihydrofolate reductase ternary complexes reduced with nicotinamide adenine dinucleotide phosphate and the very tight-binding inhibitor PT523. Biochemistry **36:**13897–13903.
19. **Cody, V., N. Galitsky, D. Rak, J. R. Luft, W. Pangborn, and S. F. Queener.** 1999. Ligand-induced conformational changes in the crystal structures of *Pneumocystis carinii* dihydrofolate reductase complexes with folate and NADP+. Biochemistry **38:**4303–4312.
20. **Cody, V., J. R. Luft, and W. Pangborn.** 2005. Understanding the role of Leu22 variants in methotrexate resistance: comparison of wild-type and Leu22Arg variant mouse and human dihydrofolate reductase ternary crystal complexes with methotrexate and NADPH. Acta Crystallogr. **D61:**147–155.
21. **Cody, V., J. Pace, K. Chisum, and A. Rosowsky.** 2006. New insights into DHFR interactions: analysis of *Pneumocystis carinii* and mouse DHFR complexes with NADPH and two highly potent 5-(omega-carboxy(alkyloxy) trimethoprim) derivatives reveals conformational correlations with activity and novel parallel ring stacking interactions. Proteins **65:**959–969.
22. **Cody, V., J. Pace, and A. Rosowsky.** 2008. Structural analysis of a holoenzyme complex of mouse dihydrofolate reductase with NADPH and a ternary complex with the potent and selective inhibitor 2,4-diamino-6-(2′-hydroxydibenz[b,f]azepin-5-yl)methylpteridine. Acta Crystallogr. D **64:**977–984.
23. **Dale, G. E., D. Broger, A. D'Arcy, P. G. Hartman, R. DeHoogt, S. Jolidon, I. Kompis, A. M. Labhardt, H. Langen, H. Locher, M. G. Page, D. Stüber, R. L. Then, B. Wipf, and C. Oefner.** 1997. A single amino acid substitution in *Staphylococcus aureus* dihydrofolate reductase determines trimethoprim resistance. J. Mol. Biol. **266:**23–30.
24. **Dann, J. G., G. Ostler, R. A. Bjur, R. W. King, P. Scudder, P. C. Turner, G. C. Roberts, and A. S. Burgen.** 1976. Large-scale purification and characterization of dihydrofolate reductase from a methotrexate-resistant strain of *Lactobacillus casei*. Biochem. J. **157:**559–571.
25. **Darrell, J. H., L. P. Garrod, and P. M. Waterworth.** 1968. Trimethoprim: laboratory and clinical studies. J. Clin. Pathol. **21:**202–209.
26. **Edman, K., A. Royant, G. Larsson, F. Jacobson, T. Taylor, D. van der Spoel, E. M. Landau, E. Pebay-Peyroula, and R. Neutze.** 2004. Deformation of helix C in the low temperature L-intermediate of bacteriorhodopsin. J. Biol. Chem. **279:**2147–2158.
27. **Emsley, P., and K. Cowtan.** 2004. Coot: model-building tools for molecular graphics. Acta Crystallogr. **D60:**2126–2132.
28. **Finland, M., and E. H. Kass.** 1973. Symposium on trimethoprim-sulfamethoxazole. J. Infect. Dis. **128:**S425–S816.
29. **Gasteiger, E., A. Gattiker, C. Hoogland, I. Ivanyi, R. D. Appel, and A. Bairoch.** 2003. ExPASy: the proteomics server for in-depth protein knowledge and analysis. Nucleic Acids Res. **31:**3784–3788.
30. **Guerry, P., C. Hubschwerlen, S. Jolidon, J.-L. Specklin, and P.-C. Wyss.** 1998. Preparation of *N*-[(2,4-diaminopyrimidinylmethyl)cinnamoyl]phthalazines as bactericides. World patent WO9839328.
31. **Guerry, P., C. Hubschwerlen, S. Jolidon, J.-L. Specklin, and P.-C. Wyss.** September, 2000. Substituted 2,4-diaminopyrimidines. U.S. patent 6,114,330.
32. **Hawser, S., S. Lociuro, and K. Islam.** 2006. Dihydrofolate reductase inhibitors as antibacterial agents. Biochem. Pharm. **71:**941–948.
33. **Hitchings, G. H., Jr.** 1989. Nobel lecture in physiology or medicine–1988. Selective inhibitors of dihydrofolate reductase. In Vitro Cell. Dev. Biol. **25:**303–310.
34. **Huovinen, P., L. Sundström, G. Swedberg, and O. Sköld.** 1995. Trimethoprim and sulfonamide resistance. Antimicrob. Agents Chemother. **39:** 279–289.
35. **Inglesby, T. V., T. O'Toole, D. A. Henderson, J. G. Bartlett, M. S. Ascher, E. Eitzen, A. M. Friedlander, J. Gerberding, J. Hauer, J. Hughes, J. McDade, M. T. Osterholm, G. Parker, T. M. Perl, P. K. Russell, and K. Tonat.** 2002. Anthrax as a biological weapon, 2002: updated recommendations for management. JAMA **287:**2236–2252.
36. **Joska, T. M., and A. C. Anderson.** 2006. Structure-activity relationships of *Bacillus cereus* and *Bacillus anthracis* dihydrofolate reductase: toward the identification of new potent drug leads. Antimicrob. Agents Chemother. **50:**3435–3443.
37. **Kongsaeree, P., P. Khongsuk, U. Leartsakulpanich, P. Chitnumsub, B. Tarnchompoo, M. D. Walkinshaw, and Y. Yuthavong.** 2005. Crystal structure of dihydrofolate reductase from *Plasmodium vivax*: pyrimethamine displacement linked with mutation-induced resistance. Proc. Natl. Acad. Sci. USA **102:**13046–13051.
38. **Li, R., R. Sirawaraporn, P. Chitnumsub, W. Sirawaraporn, J. Wooden, F. Athappilly, S. Turley, and W. G. J. Hol.** 2000. Three-dimensional structure of *Mycobacterium tuberculosis* dihydrofolate reductase reveals opportunities for the design of novel tuberculosis drugs. J. Mol. Biol. **295:**307–323.
39. **Maskell, J. P., A. M. Sefton, and L. M. Hall.** 2001. Multiple mutations modulate the function of dihydrofolate reductase in trimethoprim-resistant *Streptococcus pneumoniae*. Antimicrob. Agents Chemother. **45:**1104–1108.
40. **Molina, J. R.** 2008. Pralatrexate, a dihydrofolate reductase inhibitor for the potential treatment of several malignancies. IDrugs **11:**508–521.
41. **Nimgirawath, S.** 1994. Synthesis of (±)-isoautumnaline and (±)-dysoxyline. Aust. J. Chem. **47:**957–962.
42. **Rosowsky, A., R. A. Forsch, and S. F. Queener.** 2003. Further studies on 2,4-diamino-5-(2′,5′-disubstituted benzyl)pyrimidines as potent and selective inhibitors of dihydrofolate reductases from three major opportunistic pathogens of AIDS. J. Med. Chem. **46:**1726–1736.
43. **Rosowsky, A., R. A. Forsch, and S. F. Queener.** 2002. Inhibition of *Pneumocystis carinii*, *Toxoplasma gondii*, and *Mycobacterium avium* dihydrofolate reductases by 2,4-diamino-5-[2-methoxy-5-(omega-carboxyalkyloxy)benzyl]pyrimidines: marked improvement in potency relative to trimethoprim and species selectivity relative to piritrexim. J. Med. Chem. **45:**233–241.
44. **Sawaya, M. R., and J. Kraut.** 1997. Loop and subdomain movements in the mechanism of *Escherichia coli* dihydrofolate reductase: crystallographic evidence. Biochemistry **36:**586–603.
45. **Sirawaraporn, W., J. C. Edman, and D. V. Santi.** 1991. Purification and properties of recombinant *Pneumocystis carinii* dihydrofolate reductase. Protein Expr. Purif. **2:**313–316.
46. **Sobolev, V., A. Sorokine, J. Prilusky, E. E. Abola, and M. Edelman.** 1999. Automated analysis of interatomic contacts in proteins. Bioinformatics **15:** 327–332.
47. **Stuart, A., T. Paterson, B. Roth, and E. Aig.** 1983. 2,4-Diamino-5-benzylpyrimidines and analogues as antibacterial agents. 6. A one-step synthesis of new trimethoprim derivatives and activity analysis by molecular modeling. J. Med. Chem. **26:**667–673.
48. **Whitlow, M., A. J. Howard, D. Stewart, K. D. Hardman, J. H. Chan, D. P. Baccanari, R. L. Tansik, J. S. Hong, and L. F. Kuyper.** 2001. X-ray crystal structures of *Candida albicans* dihydrofolate reductase: high resolution ternary complexes in which the dihydronicotinamide moiety of NADPH is displaced by an inhibitor. J. Med. Chem. **44:**2928–2932.
49. **Whitlow, M., A. J. Howard, D. Stewart, K. D. Hardman, L. F. Kuyper, D. P. Baccanari, M. E. Fling, and R. L. Tansik.** 1997. X-ray crystallographic studies of *Candida albicans* dihydrofolate reductase: high-resolution structures of the holoenzyme and an inhibited ternary complex. J. Biol. Chem. **272:**30289–30298.
50. **Whitmore, F. C., H. Mosher, R. R. Adams, R. B. Taylor, E. C. Chapin, C. Weisel, and W. Yanko.** 1944. Basically substituted aliphatic nitriles and their catalytic reduction to amines. J. Am. Chem. Soc. **66:**725–731.
51. **Zinner, S. H.** 2007. Antibiotic use: present and future. New Microbiol. **30:**321–325.